# Geophysical Research Letters®

## Free Energies of Fe-O-Si Ternary Liquids at High Temperatures and Pressures: Implications for the Evolution of the Earth's Core Composition

**Zhigang Zhang**[1,2] ⬥, **Gábor Csányi**[3], **Dario Alfè**[4,5], **Yigang Zhang**[1,2], **Juan Li**[1,2] ⬥, **and Jin Liu**[6,7] ⬥

[1]Key Laboratory of Earth and Planetary Physics, Institute of Geology and Geophysics, Chinese Academy of Sciences, Beijing, China, [2]Key Laboratory of Computational Geodynamics, College of Earth and Planetary Sciences, University of Chinese Academy of Sciences, Beijing, China, [3]Department of Engineering, University of Cambridge, Cambridge, UK, [4]Department of Earth Sciences and London Centre for Nanotechnology, University College London, London, UK, [5]Dipartimento di Fisica "Ettore Pancini," Università Degli Studi di Napoli "Federico II," Complesso di Monte S. Angelo, Napoli, Italy, [6]Center for High Pressure Science and Technology Advanced Research, Beijing, China, [7]CAS Center for Excellence in Deep Earth Science, Guangzhou, China

**Abstract**  Solubility of oxygen and silicon in the iron-alloying liquids is important for constraining the core composition over the Earth's history. In this study, we systematically simulated the free energies of Fe-O-Si ternary liquids from 3000 K, 55 GPa to 6000 K, and 330 GPa. We found that temperature and pressure have remarkable influences on the free energies, and the nonideality of mixing is important for the chemical potentials even at high temperatures. Equilibrating with $SiO_2$ phase, Fe-O-Si liquids significantly enhance the solubility of Si and O simultaneously with increasing temperature. Considering the secular cooling of the Earth's core, this leads to high precipitation rates of $SiO_2$ once it was saturated, which would efficiently drive ancient geodynamo. If the evolution of Earth's core started from an oxygen-poor composition, later incorporations of oxygen seem to be needed to reach a core composition compatible with geophysical observations.

**Plain Language Summary**  According to planetary formation models, the Earth's core experienced two stages in its history: during the early stage of accretion, the iron-rich core gained light elements from the silicate mantle at high temperatures; in the subsequent stage of evolution, the core gradually cooled down and this might have led to changes in core composition. During these two stages, solubility of light elements in liquid iron determines their gain and loss limits and thus is of fundamental importance. In this study, we obtained the free energies of Fe-O-Si liquids and predicted the exsolution boundaries of $SiO_2$. The derived data show that Si and O would be precipitated out of the core as $SiO_2$ crystals at the core-mantle boundary with the secular cooling of the Earth's core, because the temperature effects are more significant than previous empirical extrapolations. With the predicted exsolution boundaries at various temperatures, we were able to provide new constraints on how the Earth's core evolved from the previous accretion stage to the present-day status.

## 1. Introduction

The Earth's core is believed to have completely formed to the current shape within the first 100 million years (Ma) after the origin of the Solar System, through a series of catastrophic collisions of planetesimals and accompanying core-mantle differentiation (Stevenson, 2008). During the growth of the Earth, the iron-rich core re-equilibrated with the silicate mantle and extracted a few light elements into it (Wood et al., 2006). While many early studies assumed that the accreted core composition would essentially remain the same in the subsequent evolution history, recent studies found critical clues on the possible changes of core composition that may be induced by the secular cooling of the Earth's core (Hirose et al., 2017; O'Rourke & Stevenson, 2016; Wahl & Militzer, 2015). From these studies, the initially dissolved elements in the iron-alloying liquids at high temperatures would be gradually exsolved out as various oxides or silicates when the core was cooled down. More importantly, the precipitation of these buoyant phases might act as efficient driving forces for the paleomagnetic field of the ancient Earth (Hirose et al., 2017; Liu et al., 2020; Mittal et al., 2020; O'Rourke & Stevenson, 2016), which would reasonably tackle the "new core paradox" before nucleation of the inner core (Olson, 2013).

Fe-O-Si is a prototype ternary system for the Earth's core composition. According to the combined constraints from mineral physics and geophysical observations, oxygen and silicon would be the major light elements in the Earth's outer core (Badro et al., 2014, 2015). Using state-of-the-art high-temperature and high-pressure experimental techniques, Hirose et al. (2017) found that the soluble regime of $SiO_2$ in the iron-alloying liquid is much more limited than previously expected under core-mantle boundary (CMB) conditions, which would provide important constraint on the evolution of the Earth's core composition as mentioned above. Nevertheless, due to the extreme challenges in such measurements, controversies still exist, and the phase relations of Fe-O-Si deserve more studies with independent approaches (Arveson et al., 2019; Huang et al., 2019).

To understand the compositional evolution of the Earth's core and the possible exsolution of light elements from the core, free energies of iron alloying liquids are important since they provide a way to uncover phase behaviors from fundamental thermodynamic principles. In this study, we first applied our recently proposed accurate and efficient first-principles method of predicting free energies to Fe-O-Si ternary liquids. Then with the analysis of these data using thermodynamics of solutions, we inspected the mixing behaviors and obtained chemical potentials, which were further used to predict the exsolution boundaries of $SiO_2$ in Fe-O-Si liquids. Applying these data, we finally discussed the compositional evolution of the core and $SiO_2$ exsolution as a driving force for the Earth's geodynamo.

## 2. Methods

### 2.1. Free Energy Calculations

To obtain free energies of Fe-O-Si liquids, we essentially followed the framework proposed in our previous study, by using a toolkit consisting of density functional theory (DFT), high-accuracy machine learning potentials and rigorous free energy calculations (Zhang et al., 2020). The details of our calculations can be found in Text S1 in Supporting Information S1. We briefly sketch the principal points below for a more general description of the techniques.

Over temperatures ($T$) of 3000–6000 K and compositions ($X$) of 0–20 mol% oxygen and silicon, at each selected $T$ and volume ($V$), we calculated the Helmholtz free energy ($F$) of the liquid through the rigorous thermodynamic integration (TI) method (Allen & Tildesley, 1987). This method involves choosing an appropriate reference state with free energy $F_0$ and a number of simulations to quantify the free energy difference through integration along the path with a coupling parameter $\lambda$, that is, $\Delta F \equiv F - F_0 = \int_0^1 \frac{\partial F_\lambda}{\partial \lambda} d\lambda$. A common reference state for a liquid is the noninteraction ideal gas at the same $T$-$V$-$X$ condition and its free energy $F_0$ can be straightforwardly calculated with the formula from statistical mechanics (McQuarrie, 1976; Zhang et al., 2020), which can be found in Text S1 in Supporting Information S1. From this referenced ideal gas, by gradually counting the interactions with the coupling parameter $\lambda$, we can obtain the $\Delta F$ and then the free energy $F$. Practically this often turns out to be a challenge, since sufficient samplings of accurate energies and forces are always demanding but prerequisite for reliable predictions through atomic level simulations.

For the iron-alloying systems, previous studies of DFT simulations have shown the importance of including more valence electrons to predict accurate phase behaviors (Sun et al., 2018). DFT simulations with these pseudopotentials further need much higher precision settings to achieve converged results. Thus, it would be infeasible to use direct DFT simulations to obtain accurate $\Delta F$ of the ternary liquids over wide $T$-$P$-$X$ conditions. In our previous effort (Zhang et al., 2020), we have shown that the machine-learning-type Gaussian Approximation Potentials (GAP) (Bartok et al., 2010) can reproduce the high precision first principles simulation results of iron-alloying systems with unprecedented accuracy. With at least three orders of magnitude speedup, they can serve as surrogate models in place of DFT to explore the phase spaces much more efficiently. Combined with the TI method mentioned above, the GAP models have been demonstrated to predict accurate melting curves and partition coefficients that are in good agreement with experiments (Zhang et al., 2020). In this study, as described in Text S1 in Supporting Information S1, we carefully trained new GAP models for Fe-O-Si liquids from small set of high precision DFT targets and then carried out extensive molecular dynamics (MD) simulations to obtain high-quality free energy data for the ternary liquids.

## 2.2. Thermodynamics of Solutions

For the ternary Fe-O-Si system, the activity coefficients can be modeled with the following extended Wagner $\varepsilon$ formulae (Ma, 2001)

$$
\begin{aligned}
\ln \gamma_{\mathrm{Fe}} = {} & \varepsilon_{\mathrm{O}}^{\mathrm{O}}(x_{\mathrm{O}} + \ln(1 - x_{\mathrm{O}})) + \varepsilon_{\mathrm{Si}}^{\mathrm{Si}}(x_{\mathrm{Si}} + \ln(1 - x_{\mathrm{Si}})) + \varepsilon_{\mathrm{Si}}^{\mathrm{O}} x_{\mathrm{O}} x_{\mathrm{Si}}\left(1 - \frac{1}{1 - x_{\mathrm{O}}} - \frac{1}{1 - x_{\mathrm{Si}}}\right) \\
& - \frac{\varepsilon_{\mathrm{Si}}^{\mathrm{O}}}{2} x_{\mathrm{O}}^2 x_{\mathrm{Si}}^2 \left(\frac{3}{1 - x_{\mathrm{O}}} + \frac{3}{1 - x_{\mathrm{Si}}} + \frac{x_{\mathrm{O}}}{(1 - x_{\mathrm{O}})^2} + \frac{x_{\mathrm{Si}}}{(1 - x_{\mathrm{Si}})^2} - 3\right)
\end{aligned}
\tag{1}
$$

$$
\begin{aligned}
\ln \gamma_{\mathrm{O}} = {} & \ln \gamma_{\mathrm{Fe}} + \ln \gamma_{\mathrm{O}}^0 - \varepsilon_{\mathrm{O}}^{\mathrm{O}} \ln(1 - x_{\mathrm{O}}) - \varepsilon_{\mathrm{Si}}^{\mathrm{O}} x_{\mathrm{Si}}\left(1 + \frac{\ln(1 - x_{\mathrm{Si}})}{x_{\mathrm{Si}}} - \frac{1}{1 - x_{\mathrm{O}}}\right) \\
& + \varepsilon_{\mathrm{Si}}^{\mathrm{O}} x_{\mathrm{Si}}^2 x_{\mathrm{O}}\left(\frac{1}{1 - x_{\mathrm{O}}} + \frac{1}{1 - x_{\mathrm{Si}}} + \frac{x_{\mathrm{O}}}{2(1 - x_{\mathrm{O}})^2} - 1\right)
\end{aligned}
\tag{2}
$$

$$
\begin{aligned}
\ln \gamma_{\mathrm{Si}} = {} & \ln \gamma_{\mathrm{Fe}} + \ln \gamma_{\mathrm{Si}}^0 - \varepsilon_{\mathrm{Si}}^{\mathrm{Si}} \ln(1 - x_{\mathrm{Si}}) - \varepsilon_{\mathrm{Si}}^{\mathrm{O}} x_{\mathrm{O}}\left(1 + \frac{\ln(1 - x_{\mathrm{O}})}{x_{\mathrm{O}}} - \frac{1}{1 - x_{\mathrm{Si}}}\right) \\
& + \varepsilon_{\mathrm{Si}}^{\mathrm{O}} x_{\mathrm{O}}^2 x_{\mathrm{Si}}\left(\frac{1}{1 - x_{\mathrm{Si}}} + \frac{1}{1 - x_{\mathrm{O}}} + \frac{x_{\mathrm{Si}}}{2(1 - x_{\mathrm{Si}})^2} - 1\right)
\end{aligned}
\tag{3}
$$

where $\gamma$ are the activity coefficients; $\gamma_{\mathrm{O}}^0$ and $\gamma_{\mathrm{Si}}^0$ are those in an infinitely dilute solution (i.e., approaching pure iron); $x_{\mathrm{O}}$ and $x_{\mathrm{Si}}$ are the mole fraction of oxygen and silicon; $\varepsilon_{\mathrm{O}}^{\mathrm{O}}$, $\varepsilon_{\mathrm{Si}}^{\mathrm{Si}}$ and $\varepsilon_{\mathrm{Si}}^{\mathrm{O}}$ are the interaction parameters.

The chemical potentials $\mu$ can then be calculated by

$$
\mu_{\mathrm{Fe}} = \bar{\mu}_{\mathrm{Fe}} + k_{\mathrm{B}}T \ln(1 - x_{\mathrm{O}} - x_{\mathrm{Si}}) = \mu_{\mathrm{Fe}}^0 + k_{\mathrm{B}}T \ln \gamma_{\mathrm{Fe}} + k_{\mathrm{B}}T \ln(1 - x_{\mathrm{O}} - x_{\mathrm{Si}})
\tag{4}
$$

$$
\mu_{\mathrm{O}} = \bar{\mu}_{\mathrm{O}} + k_{\mathrm{B}}T \ln x_{\mathrm{O}} = \mu_{\mathrm{O}}^{\ominus} + k_{\mathrm{B}}T \ln \gamma_{\mathrm{O}} + k_{\mathrm{B}}T \ln x_{\mathrm{O}}
\tag{5}
$$

$$
\mu_{\mathrm{Si}} = \bar{\mu}_{\mathrm{Si}} + k_{\mathrm{B}}T \ln x_{\mathrm{Si}} = \mu_{\mathrm{Si}}^{\ominus} + k_{\mathrm{B}}T \ln \gamma_{\mathrm{Si}} + k_{\mathrm{B}}T \ln x_{\mathrm{Si}}
\tag{6}
$$

where $\bar{\mu}$ is the quantity well behaved for all concentrations that avoids the logarithmic divergence in the low-concentration limit (Alfe et al., 2002; Zhang et al., 2020); $\mu_{\mathrm{Fe}}^0$ is the chemical potential of pure iron at the same temperature and pressure, which is the Gibbs free energy per atom of pure iron; similarly, $\mu_{\mathrm{O}}^{\ominus}$ and $\mu_{\mathrm{Si}}^{\ominus}$ are the (hypothetical) chemical potentials of pure oxygen and silicon, but practically it is more convenient to use the following auxiliary parameters which combine them with $\gamma_{\mathrm{O}}^0$ and $\gamma_{\mathrm{Si}}^0$ appeared in Equations 2 and 3

$$
\mu_{\mathrm{O}}^{\dagger} = \mu_{\mathrm{O}}^{\ominus} + k_{\mathrm{B}}T \ln \gamma_{\mathrm{O}}^0
\tag{7}
$$

$$
\mu_{\mathrm{Si}}^{\dagger} = \mu_{\mathrm{Si}}^{\ominus} + k_{\mathrm{B}}T \ln \gamma_{\mathrm{Si}}^0
\tag{8}
$$

Now the Gibbs free energy ($G$) of the whole ternary system can be calculated through

$$
\begin{aligned}
\frac{G}{N k_{\mathrm{B}}T} = {} & \frac{1}{N k_{\mathrm{B}}T}[N_{\mathrm{O}}\mu_{\mathrm{O}} + N_{\mathrm{Si}}\mu_{\mathrm{Si}} + N_{\mathrm{Fe}}\mu_{\mathrm{Fe}}] \\
= {} & \frac{1}{k_{\mathrm{B}}T}[x_{\mathrm{O}}\mu_{\mathrm{O}} + x_{\mathrm{Si}}\mu_{\mathrm{Si}} + (1 - x_{\mathrm{O}} - x_{\mathrm{Si}})\mu_{\mathrm{Fe}}] \\
= {} & \frac{1}{k_{\mathrm{B}}T}\left[x_{\mathrm{O}}\mu_{\mathrm{O}}^{\dagger} + x_{\mathrm{Si}}\mu_{\mathrm{Si}}^{\dagger} + (1 - x_{\mathrm{O}} - x_{\mathrm{Si}})\mu_{\mathrm{Fe}}^0\right] \\
& + x_{\mathrm{O}}\ln x_{\mathrm{O}} + x_{\mathrm{Si}}\ln x_{\mathrm{Si}} + (1 - x_{\mathrm{O}} - x_{\mathrm{Si}})\ln(1 - x_{\mathrm{O}} - x_{\mathrm{Si}}) \\
& + \varepsilon_{\mathrm{O}}^{\mathrm{O}}[x_{\mathrm{O}} + (1 - x_{\mathrm{O}})\ln(1 - x_{\mathrm{O}})] + \varepsilon_{\mathrm{Si}}^{\mathrm{Si}}[x_{\mathrm{Si}} + (1 - x_{\mathrm{Si}})\ln(1 - x_{\mathrm{Si}})] \\
& + \varepsilon_{\mathrm{Si}}^{\mathrm{O}}\left[\frac{1}{2}x_{\mathrm{Si}}^2 x_{\mathrm{O}}^2\left(\frac{1}{1 - x_{\mathrm{O}}} + \frac{1}{1 - x_{\mathrm{Si}}} - 1\right) - x_{\mathrm{O}}x_{\mathrm{Si}} - x_{\mathrm{O}}\ln(1 - x_{\mathrm{Si}})\right. \\
& \left. - x_{\mathrm{Si}}\ln(1 - x_{\mathrm{O}})\right]
\end{aligned}
\tag{9}
$$
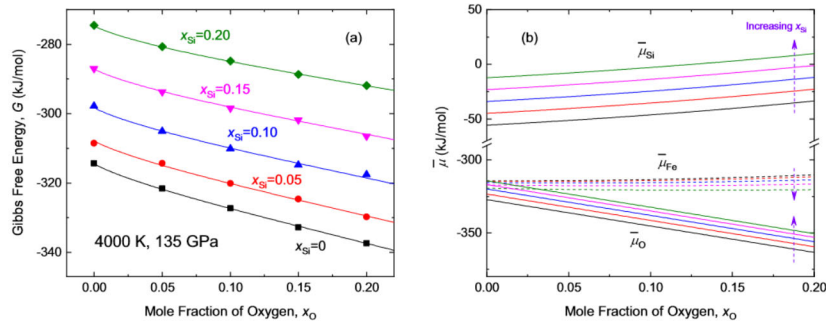
**Figure 1.** (a) Gibbs free energies $G$ and (b) $\bar{\mu}$ of Fe-O-Si ternary liquids at 4000 K, 135 GPa. The uncertainties of the simulated $G$ are generally within the sizes of the symbols. The regressed parameters for the curves in the figure can be found in Figure S2 in Supporting Information S1.

where $N = N_{Fe} + N_O + N_{Si}$ is the total number of atoms. It is straightforward to find that when oxygen or silicon is absent, Equation 9 reduces to the Gibbs free energy equation in Zhang et al. (2020), which was derived from a different route and is specific for the binaries.

At each temperature and pressure, with the simulated free energies at various concentrations of $x_O$ and $x_{Si}$, we can regress the effective values of the parameters in Equation 9 (i.e., $\mu_O^\dagger$, $\mu_{Si}^\dagger$, $\epsilon_O^O$, $\epsilon_{Si}^{Si}$, $\epsilon_{Si}^O$) and the chemical potentials can be calculated thereafter with Equations 4–6 to facilitate the discussions of phase behaviors.

## 3. Results

Through extensive simulations, we have obtained 117 records of directly simulated free energies. In addition, at each $T$ and $X$ condition, we further carried out more MD simulations and obtained 609 records of $P$-$V$-$T$-$X$ data. All these raw data can be found in the online data repository: https://doi.org/10.5281/zenodo.5912087. With these data, we were able to accurately predict the free energies and chemical potentials in Fe-O-Si liquids over a wide range of $T$-$P$-$X$ conditions.

In Figure 1a, we show the simulated Gibbs free energies at 4000 K and 135 GPa. It is obvious that impurities of silicon and oxygen have opposite effects on the total free energies under this condition. The addition of silicon up to 20 mol% into the system generally increases $G$ by up to 39–46 kJ/mol, while the same amount of oxygen would decrease $G$ by up to 17–24 kJ/mol. As shown with curves in Figure 1a, these data can be well represented with Equation 9 and the quantities related with chemical potentials can then be evaluated self-consistently through Equations 1–6 (the regressed parameters are listed in Table S2 in Supporting Information S1 along with those under other $T$-$P$ conditions). In Figure 1b, $\bar{\mu}$ shows clear compositional dependence: increasing $x_{Si}$ results in an increment of $\bar{\mu}_{Si}$ and $\bar{\mu}_O$ up to 44 kJ/mol and 13 kJ/mol, respectively; on the other hand, while the increasing of $x_O$ also increases $\bar{\mu}_{Si}$ by up to 22 kJ/mol, it noticeably decreases $\bar{\mu}_O$ by up to 37 kJ/mol.

The effects of silicon and oxygen can be greatly modulated by temperature and pressure. In Figure S2 in Supporting Information S1, we illustrate the results under around the two ends of the $T$-$P$ conditions explored in this study. At 3000 K and 55 GPa, which is a typical core-mantle separation $T$-$P$ condition (Wade & Wood, 2005; Fischer et al., 2015), both silicon and oxygen increase the total free energy by up to 35–40 kJ/mol and 9–14 kJ/mol, respectively. Under the typical inner core boundary (ICB) condition of 6000 K and 330 GPa (Alfe et al., 2002), at each composition of silicon 20 mol% oxygen remarkably decreases the free energy by 86–98 kJ/mol. Across these two conditions, the chemical potential of silicon is increased by more than 1100 kJ/mol while that of oxygen only increases by almost half that amount. In fact, the partial volume of oxygen ($v_O$) is much smaller than those
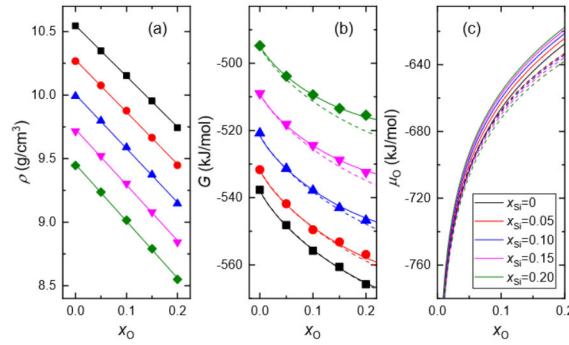
**Figure 2.** (a) Densities $\rho$, (b) Gibbs free energies $G$, and (c) chemical potential of oxygen $\mu_O$ for various mole fractions of oxygen ($x_O$) and silicon ($x_{Si}$) at 6000 K and 135 GPa. The uncertainties of the simulated data are generally within the sizes of the symbols. The solid lines are linear fits in (a), regressed curves using Equation 9 in (b) and calculated curves using Equation 5 in (c) with parameters listed in Table S2 in Supporting Information S1. The dashed lines are the results calculated by fixing $\varepsilon_{Si}^O = 0$.

of silicon and iron in the iron-alloying systems (Alfe et al., 2002) and since $d\mu = v dP$, at each temperature the chemical potential of oxygen would always become smaller than those of silicon and iron under high pressures.

The compositional dependence of $\bar{\mu}$ at various $T$-$P$ conditions noticed above implies that the ideal-mixing assumption is inadequate to fully capture the thermodynamics of the iron-alloying solutions under Earth's core conditions. Since the densities seem to keep in good linearity over the compositions from binaries to ternaries, which is revealed in Figure 2a and consistent with previous findings (Badro et al., 2014; Huang et al., 2019), the deviation from ideal mixing should be related to the energetic interactions between the impurities in the solutions and reflected by the interaction parameters in Equations 1–3 and 9, that is, $\varepsilon_O^O$, $\varepsilon_{Si}^{Si}$ and $\varepsilon_{Si}^O$. While variations of $\bar{\mu}$ as observed in Figure 1 and Figure S2 in Supporting Information S1 can be mostly ascribed to the nonzero values of $\varepsilon_O^O$ and $\varepsilon_{Si}^{Si}$, Figures 2b and 2c show the effects of the remaining unlike-interaction parameter $\varepsilon_{Si}^O$. Even under such a high temperature and relatively low pressure of 6000 K and 135 GPa, we found the role of $\varepsilon_{Si}^O$ may still be noticeable for the free energies of concentrated solutions, especially when both $x_O$ and $x_{Si}$ are larger than 0.10. The chemical potentials are more sensitive to $\varepsilon_{Si}^O$, as revealed by the opposite effects of $x_{Si}$ on $\mu_O$ in Figure 2c. Discarding $\varepsilon_{Si}^O$ may result in an underestimation of $\mu_O$ by up to over 20 kJ/mol. Under the other conditions explored in this study, since the three interaction parameters of $\varepsilon_O^O$, $\varepsilon_{Si}^{Si}$ and $\varepsilon_{Si}^O$ are even larger in magnitude, direct simulations for the ternary are indispensable to accurately depict its free energies.

With the obtained free energies and chemical potentials, it is possible to predict relevant phase behaviors from fundamental thermodynamic principles. In Figure 3, we illustrate the determinations of $SiO_2$ exsolution boundaries in Fe-O-Si liquids, which are controlled by

$$\mu_{Si}^{met} + 2\mu_O^{met} = \mu_{SiO_2} \tag{10}$$

where the superscript "met" is the liquid Fe-O-Si metal and $SiO_2$ is the exsolved phase that may be stishovite, $\beta$-stishovite, seifertite, pyrite-type, or even melt in the $T$-$P$ regime of this study (Andrault et al., 2020; Das et al., 2020; Fischer et al., 2018). As described in Text S2 in Supporting Information S1, we carried out several DFT simulations for free energies of $SiO_2$ phases at 55 and 135 GPa. In agreement with previous simulations, stishovite and seifertite are found to be the stable phases of $SiO_2$ in Figures 3a and 3b and 3c and 3d, respectively. By finding the crossover points of their chemical potentials (the Gibbs free energies per formula $SiO_2$) with $\mu_{Si} + 2\mu_O$ in the Fe-O-Si liquids (Figures 3a and 3c), we obtained the exsolution boundaries of $SiO_2$ in Figures 3b and 3d.
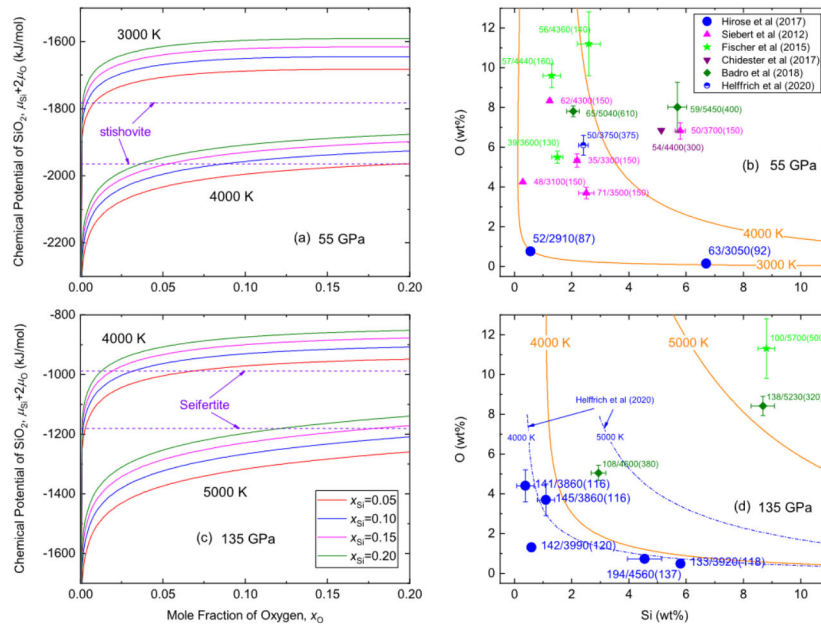
**Figure 3.** Predictions of $SiO_2$ exsolution boundaries in Fe-O-Si liquids at 55 GPa (a,b) and 135 GPa. In (a) and (c), we show $\mu_{Si}^{met} + 2\mu_{O}^{met}$ under various mole fractions of oxygen ($x_O$) and silicon ($x_{Si}$) with solid curves and $\mu_{SiO_2}$ with dashed purple lines. In (b) and (d), each experimental point is labeled with the format of $P/T$ (reported uncertainty of $T$). The data points reported by Hirose et al. (2017) are emphasized with larger symbols since they are the only data with the same exsolved phase ($SiO_2$) as our simulations. Blue dash-dotted curves in (d) are the boundaries predicted by Helffrich et al. (2020).

A number of experimental data exist for the solubility limits of silicates in iron-alloying liquids (refer to Helffrich et al. (2020) and Hirose et al. (2017) and their compilations of data). Considering the uncertainties of experimental pressure (typically ±10%) and possible systematic errors in the DFT simulations of $\mu_{SiO_2}$ (15–19 GPa according to Das et al., 2020), we include the experiment data points with pressures of 55 ± 20 GPa in Figure 3b and all the available experimental data with pressure larger than 100 GPa in Figure 3d (Badro et al., 2018; Chidester et al., 2017; Fischer et al., 2015; Helffrich et al., 2020; Hirose et al., 2017; Siebert et al., 2012). It should be noted that the deviations between different data sets may be noticeable at similar conditions. For instance, while Fischer et al. (2015) reported 1.3 ± 0.3 wt% Si and 9.6 ± 0.6 wt% O in the metal at 4440 K and 57 GPa, Chidester et al. (2017) obtained a distinct composition of 5.13 ± 0.01 wt% Si and 6.86 ± 0.02 wt% O at 4400 K and 54 GPa. This should be related with the different silicate compositions in their experiments. Since our simulations are fully independent from experiments, it is remarkable that the predicted exsolution boundaries are generally in good agreement with these measurements, especially with those reported by Hirose et al. (2017), which is the only data set with the same exsolved phase ($SiO_2$) as our simulations.

One prominent feature in Figures 3b and 3d is that increasing temperature would significantly extend the soluble regime of Fe-O-Si liquids. In fact, this has also been observed and emphasized in previous experiments by noticing the greatly increased mutual compatibility of Si and O in metal at high $T$-$P$ conditions (Fischer et al., 2015; Siebert et al., 2012). From our calculations mentioned above, it can be understood from Figures 3a and 3c by the
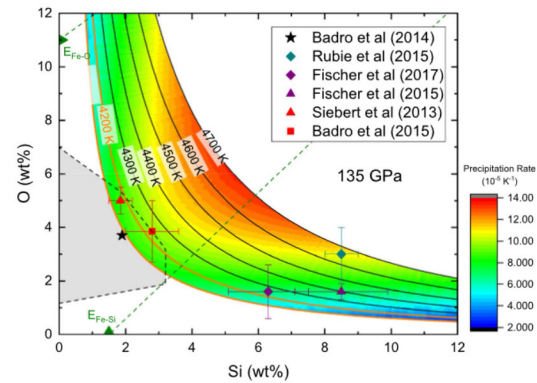
**Figure 4.** Compositions of Si and O in the outer core and the exsolutions of $SiO_2$ under 135 GPa and different temperatures. The precipitation rate of $SiO_2$ (in unit of $10^{-5}$ of Earth core mass per K), if it occurred, can be read from the colored contour at the corresponding composition. The shaded area in the black dashed lines is defined by the constraints from mineral physics and seismic observations (Badro et al., 2014, 2015). The black star within the shaded area is the best numerical solution of light elements in the current outer core (Badro et al., 2014). The green triangles noted on the two axes are the eutectic points ($E_{Fe-O}$ and $E_{Fe-Si}$) of Fe-O and Fe-Si binaries (Morard et al., 2017; Ozawa et al., 2016) and two dashed green lines connect them with the far end point of $SiO_2$ (i.e., 53.26 wt% Si and 46.74 wt% O). The remaining solid symbols in the figure are the compositions from various geochemical accretion models.

unequal temperature effects on the chemical potentials of different phases. At 135 GPa for example, the Gibbs free energy of seifertite decreases by about 193 kJ/mol from 4000 to 5000 K (Figure 3c). In contrast, $\mu_{Si} + 2\mu_O$ in the Fe-O-Si liquids decreases by at least 288 kJ/mol (a factor of 1.5; Figure 3c) with the same temperature increase, which means the iron-alloying liquid can accommodate much more silicon and oxygen at higher temperatures. Thermodynamically, since $d\mu = -sdT$, this can be further ascribed to the higher entropic effects in metallic liquids due to thermal electronic excitations (Alfe et al., 2002; Zhang et al., 2020). As a comparison, we include the boundaries predicted by a recent thermodynamic model in Figure 3d (Helffrich et al., 2020). While both boundaries at 4000 K are in rough agreement, our prediction of solubility at 5000 K is much higher than the output of the thermodynamic model. The discrepancy here may be related not only to the lack of accurate high temperature constraints but also to the aforementioned scattered experimental data, which may be involved in the empirical thermodynamic modellings.

## 4. Discussion

The significant temperature effects as noticed in Figure 3 imply that the solubilities of Si and O would be greatly enhanced in deeper areas of the Earth's outer core. This can be quantitatively revealed in Figure S3 in Supporting Information S1, which shows the predicted $SiO_2$ exsolution boundaries along the adiabatic geotherm of Earth's outer core. Assuming the liquid outer core is homogeneous in composition for the sake of low viscosity and violent convections, the exsolution of $SiO_2$ in the Earth's core, if it really happens, should more readily take place at around CMB. As pointed out by Hirose et al. (2017) and Liu et al. (2020), precipitations of oxides at CMB produce denser residual iron liquid that would sink into the deeper core and help to drive core convection.

Focusing on CMB again in Figure 4, by interpolating the simulated free energies of seifertite and Fe-O-Si liquids with appropriate EOSs (details can be found in Text S2 and Text S3 in Supporting Information S1, respectively), we obtained the exsolution curves of $SiO_2$ from 4100 to 4700 K that may be relevant to the compositions of Si and O in current and ancient Earth's core. According to Badro et al. (2014); Badro et al. (2015), to fulfill the geophysically observed densities and velocities of CMB and ICB, the possible amounts of Si and O in the current

outer core should be broadly enclosed by the black dashed region and the "best" composition would be around 1.9 wt% Si and 3.7 wt% O (the black star in Figure 4). It is important to find that these estimations are generally compatible with the soluble region defined in this study for the current CMB temperature that seems to lie between 4100 and 4200 K (Fiquet et al., 2010; Nimmo, 2015a; Stixrude et al., 2009) (i.e., on the left and down side of the orange curves in Figure 4).

In Figure 4, we also included several typical estimations of Si and O compositions from various geochemical accretion models. By different assumptions on the accretion paths, the resulting compositions are nonunique, and they can be roughly classified into two groups: one with more silicon and less oxygen (Fischer et al., 2015, 2017; Rubie et al., 2015) ("oxygen-poor scenario"), and the other one with less silicon and more oxygen (Siebert et al., 2013) ("oxygen-rich scenario"). If we consider all these compositions from accretion procedure of ancient Earth as the starting compositions for the subsequent evolution processes, it is expected that $SiO_2$ would gradually be precipitated out with the secular cooling of Earth's core. As shown in Figure 4, the starting precipitation temperature can be found from the exsolution curve passing through the initial composition. With the composition ($8.5 \pm 0.5$ wt% Si and $3.0 \pm 1.0$ wt% O) proposed by Rubie et al. (2015) as an example, it would be undersaturated until the temperature was cooled down to about 4660 K and then the outer core would keep crystallizing $SiO_2$ in the following history. Assuming $SiO_2$ is the only precipitated phase, from mass balance it is straightforward to obtain a high precipitation rate of over $10 \times 10^{-5}$ $K^{-1}$, which would generate strong compositional buoyancy to power the geodynamo as revealed by Hirose et al. (2017). As a matter of fact, from the colored contour as shown in Figure 4, except in extremely oxygen-depleted regime, the exsolved $SiO_2$ would always be an efficient driver for the geodynamo with such high precipitation rates (Nimmo, 2015b).

Since the onset of precipitating $SiO_2$ should produce sharp increases in paleomagnetic intensity (Mittal et al., 2020), it would be curious as for the possibility of finding such clues in the real paleomagnetic records (Biggin et al., 2009). Without rigorous self-consistent modellings of accretion and evolution, here we only present a conceptual discussion based on the results of previous studies. In Figure 4, both Rubie et al. (2015) and Fischer et al. (2017) combined N-body simulations with core-mantle segregation processes and obtained slightly different initial Si and O contents of the core. We arbitrarily averaged their compositions and obtained about 7.4 wt% Si and 2.3 wt% O. From the exsolution boundaries, $SiO_2$ would be saturated at around 4470 K with a high precipitate rate of around $8 \times 10^{-5}$ $K^{-1}$ as can be read from the contour of Figure 4. If this happened at around 2.78 Ga (Ga means one billion years) that corresponds to the abrupt increase of palaeointensity as recorded in the samples of Modipe Gabbro of Botswana (Biggin et al., 2009; Muxworthy et al., 2013), to reach the current CMB temperature of 4100–4200 K, the cooling rate of the core need only be 97–133 K $Ga^{-1}$, which is close to the current core cooling rate (may be around 50–115 K $Ga^{-1}$) (Nimmo, 2015b) and far less than the rate required to sustain the pre-inner-core geodynamo without $SiO_2$ crystallization (over 300 K $Ga^{-1}$ according to the geodynamic modellings; Hirose et al., 2017).

As measured by Ozawa et al. (2016) and Morard et al. (2017), the eutectic compositions of binary Fe-Si and Fe-O at 135 GPa are about 1.5 wt% Si and 11.0 wt% O, respectively. By connecting these two points with the composition of $SiO_2$ (53.26 wt% Si and 46.74 wt% O), we plotted two dashed green lines in Figure 4. As temperature decreases, Fe-O-Si liquids would lose $SiO_2$ following similar directions as these two lines. Obviously, it seems that the initial "oxygen-rich scenario" (Siebert et al., 2013; Badro et al., 2015) can be more straightforward to reach the present-day core composition regime (directly or through slightly exsolving $SiO_2$). But from the distribution of proposed compositions in these cases and the proposed thermal history of Earth's core by previous studies (Liu et al., 2020; Nimmo, 2015b), $SiO_2$ would be highly possible to keep undersaturated in the core during Archean eon and its precipitation would be activated only in the very latest history. On the other hand, although it seems to be more reasonable to comprehensively explain the accretions of solar system bodies (Rubie et al., 2015), the initial "oxygen-poor scenario" would find its difficulty to evolve to a final core composition compatible with geophysical observations through sole precipitations of $SiO_2$ (and other oxides [such as MgO and FeO] as well, according to Mittal et al., 2020). In particular, since it would gradually evolve into a composition with more Si than the eutectic point $E_{Fe-Si}$, which means the coexisting solid inner core would be the CsCl B2-phase of FeSi (Ozawa et al., 2016) and this would contradict with the core density deficit (Poirier, 1994). We noticed that recently Pozzo et al. (2019) and Davies et al. (2020) found oxygen tends to be incorporated into the liquid outer core. This "oxygen-in" process would be a promising route to solve the apparent dilemma. And

it further implies that deep oxygen-cycling would be even more critical not only for the Earth's core evolution but also for many interesting issues in the Earth's mantle and surface (Mao & Mao, 2020).

Besides O and Si, there are other candidates for the possible impurities in the Earth's core, such as S, C, and H (Hirose et al., 2021). These impurities would inevitably more or less decrease the allowed mass fractions of O and Si in the core to fulfill the geophysical observations (Badro et al., 2014, 2015; Umemoto & Hirose, 2020). In Figure 4, the shaded area in the black dashed lines would shrink and the black star that denotes the best numerical solution would move down and leftward if the core has some amounts of sulfur and carbon (Badro et al., 2014, 2015). The influence should be much smaller with hydrogen, since it has the smallest effects on the density and velocity of iron-alloy (Umemoto & Hirose, 2020). If the current core is still unsaturated for Si and O, it would hinder the role of precipitation $SiO_2$ as a driving force for the geodynamo in the Earth's history.

## 5. Conclusions

In this study, we systematically simulated the free energies of Fe-O-Si liquids over a wide range of temperatures and pressures. The demanding full range high-precision-DFT-level explorations in this endeavor were accomplished by using our previously established framework with the aids of machine learning potentials. With the obtained data, it is possible to derive chemical potentials without a-priori assumption of ideal mixing and thus facilitates more accurate predictions of relevant phase behaviors.

Both temperature and pressure have great effects on the free energies and chemical potentials of Fe-O-Si liquids. Increasing temperature, in particular, would significantly reduce chemical potentials of impurities in iron-alloying liquids. When being equilibrated with $SiO_2$ phase, in accord with recent experiments, Fe-O-Si liquids show a remarkably extended soluble regime for Si and O at higher temperatures from our calculations.

Based on the predicted exsolution boundaries of $SiO_2$ at various temperatures relevant to the current and ancient Earth's core, we further discussed the implications for the evolution of core composition. The strong temperature dependence as found in our results implies that excessive $SiO_2$ would be exsolved at CMB with a high precipitation rate, once it was saturated with the secular cooling of the Earth's core. So precipitating $SiO_2$ may act as an efficient driving force for the ancient geodynamo. From the predicted phase diagram, if the initial accreted core was oxygen-poor in composition, it can hardly evolve into a present-day core composition that is compatible with geophysical observations by only precipitating $SiO_2$. This would infer an "oxygen-in" process in the evolution history.

## Data Availability Statement

The data used in this study have been deposited at https://doi.org/10.5281/zenodo.5912087.

## References

Alfe, D., Gillan, M. J., & Price, G. D. (2002). Ab initio chemical potentials of solid and liquid solutions and the chemistry of the Earth's core. *Journal of Chemical Physics*, *116*(16), 7127–7136. https://doi.org/10.1063/1.1464121

Allen, M. P., & Tildesley, D. J. (1987). *Computer simulation of liquids [Book]*. Clarendon Press; Oxford University Press.

Andrault, D., Morard, G., Garbarino, G., Mezouar, M., Bouhifd, M. A., & Kawamoto, T. (2020). Melting behavior of $SiO_2$ up to 120 GPa. *Physics and Chemistry of Minerals*, *47*(2), 10. https://doi.org/10.1007/s00269-019-01077-3

Arveson, S. M., Deng, J., Karki, B. B., & Lee, K. K. M. (2019). Evidence for Fe-Si-O liquid immiscibility at deep Earth pressures. *Proceedings of the National Academy of Sciences*, *116*(21), 10238–10243. https://doi.org/10.1073/pnas.1821712116

Badro, J., Aubert, J., Hirose, K., Nomura, R., Blanchard, I., Borensztajn, S., & Siebert, J. (2018). Magnesium partitioning between Earth's mantle and core and its potential to drive an early exsolution geodynamo. *Geophysical Research Letters*, *45*(24), 13240–13248. https://doi.org/10.1029/2018gl080405

Badro, J., Brodholt, H., Piet, H., Siebert, J., & Ryerson, F. J. (2015). Core formation and core composition from coupled geochemical and geophysical constraints. *Proceedings of the National Academy of Sciences*, *112*(40), 12310–12314. https://doi.org/10.1073/pnas.1505672112

Badro, J., Côté, A. S., & Brodholt, J. P. (2014). A seismologically consistent compositional model of Earth's core. *Proceedings of the National Academy of Sciences*, *111*(21), 7542–7545. https://doi.org/10.1073/pnas.1316708111

Bartok, A. P., Payne, M. C., Kondor, R., & Csanyi, G. (2010). Gaussian approximation potentials: The accuracy of quantum mechanics, without the electrons. *Physical Review Letters*, *104*(13), 136403. https://doi.org/10.1103/Physrevlett.104.136403

Biggin, A. J., Strik, G. H. M. A., & Langereis, C. G. (2009). The intensity of the geomagnetic field in the late-Archaean: New measurements and an analysis of the updated IAGA palaeointensity database. *Earth Planets and Space*, *61*(1), 9–22. https://doi.org/10.1186/bf03352881

Chidester, B. A., Rahman, Z., Righter, K., & Campbell, A. J. (2017). Metal-silicate partitioning of U: Implications for the heat budget of the core and evidence for reduced U in the mantle. *Geochimica et Cosmochimica Acta*, *199*, 1–12. https://doi.org/10.1016/j.gca.2016.11.035

Das, P. K., Mohn, C. E., Brodholt, J. P., & Tronnes, R. G. (2020). High-pressure silica phase transitions: Implications for deep mantle dynamics and silica crystallization in the protocore. *American Mineralogist, 105*(7), 1014–1020. https://doi.org/10.2138/am-2020-7299

Davies, C. J., Pozzo, M., Gubbins, D., & Alfè, D. (2020). Transfer of oxygen to Earth's core from a long-lived magma ocean. *Earth and Planetary Science Letters, 538*, 116208. https://doi.org/10.1016/j.epsl.2020.116208

Fiquet, G., Auzende, A. L., Siebert, J., Corgne, A., Bureau, H., Ozawa, H., & Garbarino, G. (2010). Melting of peridotite to 140 gigapascals. *Science, 329*(5998), 1516–1518. https://doi.org/10.1126/science.1192448

Fischer, R. A., Campbell, A. J., Chidester, B. A., Reaman, D. M., Thompson, E. C., Pigott, J. S., et al. (2018). Equations of state and phase boundary for stishovite and CaCl$_2$-type SiO2. *American Mineralogist, 103*(5), 792–802. https://doi.org/10.2138/am-2018-6267

Fischer, R. A., Campbell, A. J., & Ciesla, F. J. (2017). Sensitivities of Earth's core and mantle compositions to accretion and differentiation processes. *Earth and Planetary Science Letters, 458*, 252–262. https://doi.org/10.1016/j.epsl.2016.10.025

Fischer, R. A., Nakajima, Y., Campbell, A. J., Frost, D. J., Harries, D., Langenhorst, F., et al. (2015). High pressure metal-silicate partitioning of Ni, Co, V, Cr, Si, and O. *Geochimica et Cosmochimica Acta, 167*, 177–194. https://doi.org/10.1016/j.gca.2015.06.026

Helffrich, G., Hirose, K., & Nomura, R. (2020). Thermodynamical modeling of liquid Fe-Si-Mg-O: Molten magnesium silicate release from the core. *Geophysical Research Letters, 47*(21), e89218. https://doi.org/10.1029/2020gl089218

Hirose, K., Morard, G., Sinmyo, R., Umemoto, K., Hernlund, J., Helffrich, G., & Labrosse, S. (2017). Crystallization of silicon dioxide and compositional evolution of the earth's core. *Nature, 543*(7643), 99–102. https://doi.org/10.1038/nature21367

Hirose, K., Wood, B., & Vočadlo, L. (2021). Light elements in the Earth's core. *Nature Reviews Earth & Environment, 2*(9), 645–658. https://doi.org/10.1038/s43017-021-00203-6

Huang, D. Y., Badro, J., Brodholt, J., & Li, Y. G. (2019). Ab initio molecular dynamics investigation of molten Fe-Si-O in Earth's core. *Geophysical Research Letters, 46*(12), 6397–6405. https://doi.org/10.1029/2019gl082722

Liu, W. Y., Zhang, Y. G., Yin, Q. Z., Zhao, Y., & Zhang, Z. G. (2020). Magnesium partitioning between silicate melt and liquid iron using first-principles molecular dynamics: Implications for the early thermal history of the Earth's core. *Earth and Planetary Science Letters, 531*, 115934. https://doi.org/10.1016/j.epsl.2019.115934

Ma, Z. T. (2001). Thermodynamic description for concentrated metallic solutions using interaction parameters. *Metallurgical and Materials Transactions B, Process Metallurgy and Materials Processing Science, 32*(1), 87–103. https://doi.org/10.1007/s11663-001-0011-0

Mao, H.-K., & Mao, W. L. (2020). Key problems of the four-dimensional Earth system. *Matter and Radiation at Extremes, 5*(3), 038102. https://doi.org/10.1063/1.5139023

McQuarrie, D. A. (1976). *Statistical mechanics*. Harper & Row Publishers Inc.

Mittal, T., Knezek, N., Arveson, S. M., McGuire, C. P., Williams, C. D., Jones, T. D., & Li, J. (2020). Precipitation of multiple light elements to power Earth's early dynamo. *Earth and Planetary Science Letters, 532*, 116030. https://doi.org/10.1016/j.epsl.2019.116030

Morard, G., Andrault, D., Antonangeli, D., Nakajima, Y., Auzende, A. L., Boulard, E., et al. (2017). Fe-FeO and Fe-Fe$_3$C melting relations at Earth's core-mantle boundary conditions: Implications for a volatile-rich or oxygen-rich core. *Earth and Planetary Science Letters, 473*, 94–103. https://doi.org/10.1016/j.epsl.2017.05.024

Muxworthy, A. R., Evans, M. E., Scourfield, S. J., & King, J. G. (2013). Paleointensity results from the late-archaean Modipe Gabbro of Botswana. *Geochemistry, Geophysics, Geosystems, 14*(7), 2198–2205. https://doi.org/10.1002/ggge.20142

Nimmo, F. (2015a). 8.02–Energetics of the core. In G. Schubert (Ed.), *Treatise on geophysics* (2nd ed., pp. 27–55). Elsevier. https://doi.org/10.1016/B978-0-444-53802-4.00139-1

Nimmo, F. (2015b). 9.08–thermal and compositional evolution of the core. In G. Schubert (Ed.), *Treatise on geophysics* (2nd ed., pp. 201–219). Elsevier. https://doi.org/10.1016/B978-0-444-53802-4.00160-3

Olson, P. (2013). The new core paradox. *Science, 342*(6157), 431–432. https://doi.org/10.1126/science.1243477

O'Rourke, J. G., & Stevenson, D. J. (2016). Powering Earth's dynamo with magnesium precipitation from the core. *Nature, 529*(7586), 387–389. https://doi.org/10.1038/nature16495

Ozawa, H., Hirose, K., Yonemitsu, K., & Ohishi, Y. (2016). High-pressure melting experiments on Fe-Si alloys and implications for silicon as a light element in the core. *Earth and Planetary Science Letters, 456*, 47–54. https://doi.org/10.1016/j.epsl.2016.08.042

Poirier, J.-P. (1994). Light elements in the earth's outer core: A critical review. *Physics of the Earth and Planetary Interiors, 85*(3), 319–337. https://doi.org/10.1016/0031-9201(94)90120-1

Pozzo, M., Davies, C., Gubbins, D., & Alfè, D. (2019). FeO content of Earth's liquid core. *Physical Review X, 9*(4), 041018. https://doi.org/10.1103/PhysRevX.9.041018

Rubie, D. C., Jacobson, S. A., Morbidelli, A., O'Brien, D. P., Young, E. D., de Vries, J., et al. (2015). Accretion and differentiation of the terrestrial planets with implications for the compositions of early-formed solar system bodies and accretion of water. *Icarus, 248*, 89–108. https://doi.org/10.1016/j.icarus.2014.10.015

Siebert, J., Badro, J., Antonangeli, D., & Ryerson, F. J. (2012). Metal-silicate partitioning of Ni and Co in a deep magma ocean. *Earth and Planetary Science Letters, 321*, 189–197. https://doi.org/10.1016/j.epsl.2012.01.013

Siebert, J., Badro, J., Antonangeli, D., & Ryerson, F. J. (2013). Terrestrial accretion under oxidizing conditions. *Science, 339*(6124), 1194–1197. https://doi.org/10.1126/science.1227923

Stevenson, D. J. (2008). A planetary perspective on the deep Earth. *Nature, 451*(7176), 261–265. https://doi.org/10.1038/Nature06582

Stixrude, L., de Koker, N., Sun, N., Mookherjee, M., & Karki, B. B. (2009). Thermodynamics of silicate liquids in the deep Earth. *Earth and Planetary Science Letters, 278*(3–4), 226–232. https://doi.org/10.1016/j.epsl.2008.12.006

Sun, T., Brodholt, J. P., Li, Y. G., & Vocadlo, L. (2018). Melting properties from ab initio free energy calculations: Iron at the Earth's inner-core boundary. *Physical Review B, 98*(22), 224301. https://doi.org/10.1103/Physrevb.98.224301

Umemoto, K., & Hirose, K. (2020). Chemical compositions of the outer core examined by first principles calculations. *Earth and Planetary Science Letters, 531*, 116009. https://doi.org/10.1016/j.epsl.2019.116009

Wade, J., & Wood, B. J. (2005). Core formation and the oxidation state of the Earth. *Earth and Planetary Science Letters, 236*(1), 78–95. https://doi.org/10.1016/j.epsl.2005.05.017

Wahl, S. M., & Militzer, B. (2015). High-temperature miscibility of iron and rock during terrestrial planet formation. *Earth and Planetary Science Letters, 410*, 25–33. https://doi.org/10.1016/j.epsl.2014.11.014

Wood, B. J., Walter, M. J., & Wade, J. (2006). Accretion of the Earth and segregation of its core. *Nature, 441*(7095), 825–833. https://doi.org/10.1038/nature04763

Zhang, Z., Csányi, G., & Alfè, D. (2020). Partitioning of sulfur between solid and liquid iron under Earth's core conditions: Constraints from atomistic simulations with machine learning potentials. *Geochimica et Cosmochimica Acta, 291*(291), 5–18. https://doi.org/10.1016/j.gca.2020.03.028

## References From the Supporting Information

Alfè, D. (2009). PHON: A program to calculate phonons using the small displacement method. *Computer Physics Communications, 180*(12), 2622–2633. https://doi.org/10.1016/j.cpc.2009.03.010

Deringer, V. L., Caro, M. A., & Csanyi, G. (2019). Machine learning interatomic potentials as emerging tools for materials science. *Advanced Materials, 31*(46), 1902765. https://doi.org/10.1002/Adma.201902765

Dorner, F., Sukurma, Z., Dellago, C., & Kresse, G. (2018). Melting Si: Beyond density functional theory. *Physical Review Letters, 121*(19), 195701. https://doi.org/10.1103/Physrevlett.121.195701

Japan Society for the Promotion of Science and the Nineteenth Committee on Steelmaking. (1988). *Steelmaking data sourcebook*. Gordon and Breach Science Publishers.

Kresse, G., & Joubert, D. (1999). From ultrasoft pseudopotentials to the projector augmented-wave method. *Physical Review B, 59*(3), 1758–1775. https://doi.org/10.1103/PhysRevB.59.1758

Mermin, N. D. (1965). Thermal properties of inhomogeneous electron gas. *Physical Review, 137*(5A), 1441–1443.

Perdew, J. P., Burke, K., & Ernzerhof, M. (1996). Generalized gradient approximation made simple. *Physical Review Letters, 77*(18), 3865–3868. https://doi.org/10.1103/PhysRevLett.77.3865